ACS APPLIED MATERIALS & INTERFACES

Research Article

Cite This: ACS Appl. Mater. Interfaces 2019, 11, 24707−24714

www.acsami.org

Oxygen Reduction Reaction Catalyzed by Black-Phosphorus-Supported Metal Nanoparticles: Impacts of Interfacial Charge Transfer

Yi Peng,[†] Bingzhang Lu,[†] Nan Wang,[§] Jia En Lu,[†] Chunhong Li,[*,†,‡] Yuan Ping,[†] and Shaowei Chen[*,†]

[†]Department of Chemistry and Biochemistry, University of California, 1156 High Street, Santa Cruz, California 95060, United States

[‡]Beijing National Laboratory for Condensed Matter Physics, Institute of Physics, Chinese Academy of Sciences, Beijing 100190, China

[§]School of Environment and Energy, New Energy Research Institute, South China University of Technology, Guangzhou Higher Education Mega Centre, Guangzhou 510006, China

Supporting Information

ABSTRACT: Development of effective catalysts for oxygen reduction reaction (ORR) plays a critical role in the applications of a range of electrochemical energy technologies. In this study, thin-layered black phosphorus (TLBP) was used as a unique supporting substrate for the deposition of metal nanoparticles (MNPs, M = Pt, Ag, Au), and the resulting M-TLBP nanocomposites were found to exhibit apparent ORR activity that was readily manipulated by interfacial charge transfer from TLBP to MNPs. This was confirmed by results from X-ray photoelectron spectroscopic measurements and density functional theory calculations. In comparison to the carbon-supported counterparts, Ag-TLBP and Au-TLBP showed enhanced ORR performance, while a diminished performance was observed with Pt-TLBP. This was consistent with the predictions from the "volcano plot". Results from this study suggest that black phosphorus can serve as a unique addition in the toolbox of manipulating electronic properties of supported metal nanoparticles and their electrocatalytic activity.

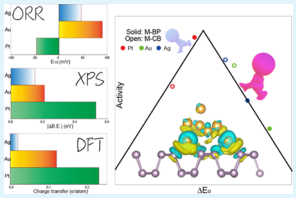

KEYWORDS: *black phosphorus, metal nanoparticle, electron transfer, oxygen reduction reaction, volcano plot*

INTRODUCTION

Oxygen reduction reaction (ORR) is a critical process in a variety of electrochemical energy technologies, such as polymer electrolyte membrane fuel cells and metal−air batteries, where the device performance is largely dictated by the sluggish electron-transfer kinetics of ORR.[1−3] Thus, the design and engineering of effective catalysts that facilitate oxygen reduction are of both fundamental and technological significances.[4,5] Toward this end, the mechanistic manipulation of the electronic interaction between oxygen intermediates and the catalyst surface represents a critical first step. In the well-known "volcano plot", it is found that the ORR activity of a range of transition metals can be correlated with the corresponding oxygen adsorption energy.[6−9] Based on this theory, for metals that bind to oxygen species too strongly (e.g., Pt, Pd, Cu), the ORR activity is not optimal because the reduction products become difficult to desorb, whereas for the metals that bind to oxygen too weakly (e.g., Au, Ag), the ORR activity is compromised because the reactant cannot be stably adsorbed onto the catalytic active sites. Platinum happens to exhibit a not-too-strong or too-weak binding to oxygen (though on the slightly strong side) and exhibits the best ORR activity among the series. Thus, the manipulation of the metal electronic properties and hence the interaction with oxygen species have become an effective strategy to regulate the ORR activity. This can be achieved by a number of approaches, such as alloying with (non)noble metals, surface functionalization with select organic ligands or ions, and deposition of metal nanoparticles on functional substrate supports.[10−16] Mechanistically, the intimate contact between the active metals and other metals/molecules/substrates leads to charge redistributions, due to effective interfacial charge transfer. For instance, according to the volcano plot, to further enhance the ORR activity of Pt, the oxygen binding energy needs to be reduced by 0.1−0.2 eV, whereas for Ag and Au, enhanced interaction with oxygen species is anticipated to lead to improved ORR activity.[6−9] Experimentally, we have indeed observed that by functionalizing platinum nanoparticles with electron-withdrawing ligands or depositing the nanoparticles onto defective graphene quantum dots (GQDs), the Pt ORR activity can be enhanced rather significantly due to charge transfer to the ligands/GQD defects.[17−20] In the present study, we demonstrate that black phosphorus (BP) can serve as another effective substrate, where the unique electronic properties can be exploited for the manipulation of the

Received: March 27, 2019
Accepted: June 14, 2019
Published: June 14, 2019

DOI: 10.1021/acsami.9b05471
ACS Appl. Mater. Interfaces 2019, 11, 24707−24714

nanoparticle ORR activity. It should be noted that this has remained largely unexplored thus far.

BP is a unique allotrope of phosphorus, featuring a lattice structure where 6-membered rings of P are interlinked with each P bonded to three others. Chemical and mechanical exfoliations can lead to the production of two-dimensional (2D) nanosheets, which differ from the graphene counterparts, in that the P atoms in BP nanosheets are not π-conjugated and thus not coplanar. In such a corrugated structure, the lone-pair electrons of P extrude from the 2D surface and hence may be involved in effective interfacial charge transfer with nanoparticles deposited on BP surface, due to high carrier mobility and high Fermi level.[21,22] For instance, it has recently been reported that by depositing MoS_2 or Ni_2P onto BP nanosheets, the electrocatalytic activity toward hydrogen evolution reaction was enhanced markedly, which was ascribed to charge transfer from BP to MoS_2 or Ni_2P that facilitated hydrogen binding to the active sites.[23,24] Similar electronic manipulation has also been observed in ethanol oxidation electrocatalysts and photocatalysts, where the BP was used as a cocatalyst in the hybrid structure.[25−29] Nevertheless, thus far, there has been no report of BP applications in ORR electrocatalysis.

Herein, Pt, Ag, or Au were selected as the illustrating examples, where their nanoparticles were formed and deposited onto thin-layered BP (M-TLBP, M = Pt, Ag or Au), and the impacts of BP on the ORR activity of the metal nanoparticles were examined and compared to those with the carbon-supported counterparts (M-CB).

EXPERIMENTAL SECTION

Chemicals. Tin powders (99.999%, Alfa Aesar), iodine (99.5%, Alfa Aesar), gold (99.999%, GRINM), red phosphorus (>99.999%, Chempur), sodium borohydride ($NaBH_4$, 99%, ACROS), platinum-(IV) chloride ($PtCl_4$, 57.0−58.5% Pt, ACROS), tetrachloroauric acid ($HAuCl_4{\cdot}4H_2O$, 99.9%, Sigma-Aldrich), and silver nitrate ($AgNO_3$, 99%, Fisher Scientific) were all used as received. Solvents were obtained from leading commercial vendors at the highest purity available and also used as received. Deionized water was supplied with a Barnstead nanopure water system (resistivity of 18.3 MΩ cm).

Synthesis of Black Phosphorus. Black phosphorous (BP) crystals were synthesized by using a modified literature method.[30,31] Briefly, SnI_4 was first prepared by refluxing 1.2 g of tin powers and 4.0 g of iodine in 25 mL of toluene until the violet color of the dissolved iodine vanished, and then the hot solution was separated from the excess tin and recrystallized at room temperature to obtain the products. Separately, AuSn was prepared by melting an equal molar amount of gold and tin in a sealed evacuated silica ampoule. The produced AuSn (364 mg), along with 500 mg of red phosphorus, was then loaded into a silica ampoule (inner diameter 10 mm and length 10 cm), into which was added 10 mg of SnI_4. After evacuation to a pressure below 10^{-3} mbar, the ampoule was sealed and placed in a muffle furnace, where the temperature program involved a rise to 400 °C within 4 h, heating at 400 °C for 2 h, a continuing rise to 600 °C within 2 h, and heating at 600 °C for 23 h. Afterward, a programmed cool-down process was applied, where the temperature was first lowered to 500 °C in 2.5 h and kept at 500 °C for 2 h and further to room temperature in 4 h, affording single-crystalline BP. To prepare thin-layered black phosphorus (TLBP), 50 mg of the as-prepared BP was first ground for 30 min and then dispersed under sonication overnight in 50 mL of *N*-methyl-2-pyrrolidone (NMP). The dispersion was diluted to 500 mL by NMP and refluxed for 6 h under a nitrogen atmosphere, corresponding to a concentration of 0.1 mg/mL TLBP in NMP.

Synthesis of BP-Supported Metal (Ag, Pt, Au) Nanoparticles. The solution of $PtCl_4$ (1 mL, 20 mg/mL), $HAuCl_4{\cdot}4H_2O$ (1 ml, 12.2 mg/mL), or $AgNO_3$ (1 mL, 30 mg/mL) in water and 50 mL of the solution of 0.1 mg/mL TLBP in NMP were mixed under vigorous stirring. The first two solutions were kept at room temperature, while the last one (containing $AgNO_3$) was cooled in an ice bath for about 30 min, before 0.5, 0.3, and 0.7 mL of freshly prepared, aqueous $NaBH_4$ solution (100 mg/mL, ice cold) was added into the above three solutions. The colors of the dispersions became dark brown, dark yellow, and dark red, respectively, from light brown in about 20 min. After magnetic stirring overnight, the products were separated by centrifugation, rinsed with an ethanol/water (v/v = 3:1) mixture, and desiccated at 60 °C in a vacuum oven. The purified products were referred to as M-TLBP (M = Pt, Au, and Ag).

As control samples, Pt, Au, and Ag nanoparticles were also prepared in the same manner except that TLBP was replaced by the desired amount of carbon black. The resulting products were denoted as M-CB.

Structural Characterizations. UV−vis measurements were conducted with a Perkin Elmer Lambda 35 UV−vis spectrometer. Transmission electron microscopic (TEM) images were acquired with a JEOL JEM 2100 F microscope. X-ray photoelectron spectra (XPS) were obtained with a PHI 5400 instrument (Al Kα radiation, 350 W, and 10^{-9} Torr). Atomic force microscopy (AFM) topographic measurements were carried out with a Molecular Imaging PicoLE SPM instrument under ambient condition. X-ray diffraction (XRD) measurements were performed with a Rigaku Americas Miniflex Plus diffractometer (Cu Kα radiation, λ = 1.5418 Å), where the 2θ angle was scanned from 10 to 80° at 2°/min.

Electrochemistry. Electrochemical measurements were conducted on a CHI 710 C workstation in the aqueous solution of 0.1 M KOH. A graphite rod was used as the counter electrode, and a Ag/AgCl (1 M KCl) electrode as the reference. The Ag/AgCl electrode was calibrated against a reversible hydrogen electrode (RHE), and all potentials in the present study were reported with reference to this RHE. Catalyst inks were prepared by mixing a calculated amount of the M-TLBP or M-CB catalysts prepared above and carbon black at the metal-to-carbon-black mass ratio of 3:7. The metal concentration was then adjusted to 1 mg/mL using a mixture of water and isopropanol (v/v 1:3) containing 1% Nafion as the solvent. After sonication of the mixture for ca. 30 min, a homogeneous catalyst ink was produced. The catalyst ink (10 μL) containing Pt nanoparticles or 20 μL for the inks containing Ag or Au nanoparticles was drop-cast onto the clean glassy carbon disk (0.246 cm^2 geometric area) of a (glassy carbon) disk-(gold) ring electrode (from Pine Instrument), followed by the addition of 5 μL of 20% Nafion. The corresponding metal loadings were 40 μg Pt/cm^2, 80 μg Ag/cm^2, and 80 μg Au/cm^2, respectively. The electrode was dried in ambient and then immersed into an electrolyte solution for voltammetric measurements.

Density Functional Theory (DFT) Calculations. First-principles computations were performed using Quantum ESPRESSO, an open-source plane-wave code.[32] A 4 × 3 unit cell with 48 atoms was used to build a 2D black phosphorus matrix supercell, where periodic image interactions were removed by setting a vacuum of 14 Å. A cutoff of 40 and 240 Ry for kinetics and charge density was chosen for the ultrasoft pseudopotential.[33] The total energy of the 5 × 5 × 1 Monkhorst−Pack *K*-point grid in the supercell was calculated at the convergence level of 1 meV per atom. The smearing parameter was set at 0.005 Ry in the Marzari Vanderbilt smearing[34] for the calculations with a metal cluster. The convergence was 10^{-8} Ry of the electronic energy and 10^{-4} au for the total force. All systems involved spin-polarized calculations, with van der Waals correction for the images containing the D2 scheme of Grimme et al.[35,36]

RESULTS AND DISCUSSION

BP was synthesized using a slightly modified literature procedure,[30] exfoliated to TLBP with an average thickness of ca. 4 layers (Figure S1) and used as supporting substrates to prepare the series of M-TLBP samples. It should be noted that whereas BP has been known to be prone to ambient degradation due to the reactive lone-pair electrons, the M-TLBP composites were actually chemically stable under

DOI: 10.1021/acsami.9b05471
ACS Appl. Mater. Interfaces 2019, 11, 24707−24714

ambient condition, most likely due to charge transfer between TLBP and metal nanoparticles.[23,24,29,37] The samples were first characterized by UV−vis spectroscopic measurements. From Figure S2, one can see that TLBP exhibited a characteristic absorption peak at about 325 nm, consistent with results from previous studies.[38,39] When the metal nanoparticles were deposited onto TLBP, the absorption profile remained largely unchanged for Pt-TLBP, but additional characteristic peaks emerged at 406 nm for Ag-TLBP and 544 nm for Au-TLBP, due to their surface plasma resonance absorption in the visible range.[40,41]

The sample structures were further examined by XRD measurements. As shown in Figure S3, TLBP exhibited four major diffraction peaks at 2θ = 16.9, 34.2, 52.4, and 72.14°, which can be assigned to the (020), (040), (060), and (080) crystalline planes of BP of orthorhombic phase (JCPDF no. 76-1957), respectively.[24] These characteristic peaks can also be found in the M-TLBP samples, signifying the stability of BP in the composite samples. For Au-TLBP and Ag-TLBP, four additional diffraction peaks can be identified at 2θ = 38.2, 44.3, 64.5, and 77.5°, due to the (111), (200), (220), and (311) crystalline planes of Au (JCPDF no. 04-0784) and Ag (JCPDF no. 04-0783), respectively,[42] whereas Pt-TLBP exhibited only two broad peaks centered at ca. 40 and 44° that likely arose from the Pt(111) and (200) diffractions (JCPDS no. 73-2360), due to the significantly diminished size of the Pt nanoparticles (Figure 1).[43]

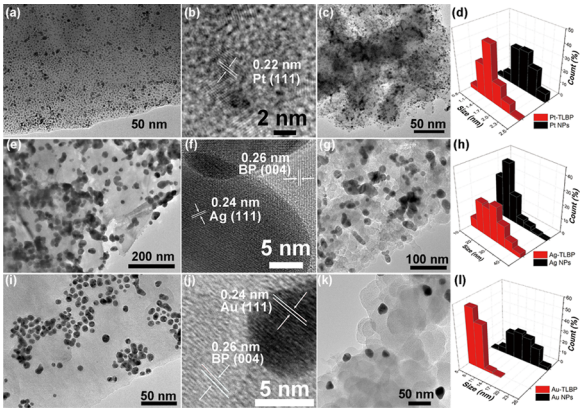

Figure 1. Representative TEM images of (a, b) Pt-TLBP, (c) Pt-CB, (e, f) Ag-TLBP, (g) Ag-CB, (i, j) Au-TLBP, and (k) Au-CB. The corresponding core size histograms are shown in (d) for Pt, (h) for Ag, and (l) for Au nanoparticles in the M-TLBP (red) and M-CB (black) series.

The morphologies of the M-TLBP samples were then studied by TEM measurements. It can be seen from Figure 1a,e,i that in the M-TLBP series, the metal nanoparticles were dispersed rather evenly on the TLBP surface without obvious agglomeration. From the high-resolution TEM images in Figure 1b,f,j, the nanoparticles can be seen to all exhibit well-defined lattice fringes with an interplanar spacing of 0.22 nm for Pt-TLB, and 0.24 nm for both Ag-TLBP and Au-TLBP, consistent with the Pt(111), Ag(111), and Au(111) crystal planes, respectively.[44−46] Additionally, the low-contrast background exhibited a larger lattice spacing of 0.26 nm that can be ascribed to the (004) planes of BP (Figure S4).[47,48] This suggests that the metal nanoparticles were indeed deposited on the TLBP surface. The corresponding nanoparticle core size histograms are depicted in Figure 1d,h,l, with an average core diameter of 1.7 ± 0.3 nm for Pt-TLBP, 25 ± 7 nm for Ag-TLBP, and 8.1 ± 1.7 nm for Au-TLBP. For comparison, when the nanoparticles were prepared in the presence of carbon black (Figure 1c,g,k) instead of TLBP, the size of the corresponding nanoparticles was somewhat larger than those of M-TLBP, 1.8 ± 0.3 nm for Pt-CB, 18 ± 5 nm for Ag-CB, and 16.4 ± 3.8 nm for Au-CB (Figure 1d,h,l).

The elemental composition and valence states of the samples were then examined by XPS measurements. Figure 2a shows the XPS spectra of the Pt 4f electrons in Pt-TLBP (top) and Pt-CB (bottom). For the Pt-CB sample, deconvolution yields two pairs of peaks at 72.02/75.37 eV and 73.81/77.16 eV. The former can be assigned to metallic Pt^0, while the latter can be contributed to Pt^{2+}.[49] Pt-TLBP also exhibited two pairs of peaks, but the binding energies red-shifted slightly. For instance, the Pt^0 $4f_{7/2}$ was identified at 71.49 eV, ca. 0.53 eV lower than that of Pt-CB. Similarly, the Au^0 $4f_{7/2}$ peak of Au-TLBP red-shifted to 84.04 eV from 84.16 eV for Au-CB (Figure 2b).[50] Different from Pt and Au, the peak position of Ag $3d_{5/2}$ actually blue-shifted from 386.31 eV for Ag-CB to 386.46 eV for Ag-TLBP (Figure 2c). It should be noted that for Ag, higher binding energy corresponds to a richer electron density.[51,52] This suggests that in the M-TLBP samples, charge transfer occurred from TLBP to the metal nanoparticles, in comparison to the M-CB counterparts. Consistent results can be obtained in XPS measurements of the P 2p electrons. From Figure 2d, TLBP alone can be seen to display a pair of peaks at 129.66/139.56 eV, which can be assigned to P^0 $2p_{3/2}/2p_{1/2}$ (a minor one at 133.13 eV likely due to oxidized P).[53,54] These binding energies all showed an apparent increase in the M-TLBP samples. For instance, the P^0 $2p_{3/2}$ peaks shifted to 129.95, 129.92, and 129.91 eV for Pt-TLBP, Ag-TLBP, and Au-TLBP, respectively. Again, this is consistent with electron transfer from TLBP to the metal nanoparticles, most probably due to the relatively high Fermi level of BP, as compared to those of the metals (Figure 2b, inset).[55,56]

Consistent results were obtained in theoretical studies based on DFT calculations. To simplify the calculations, we adopted the structural models (Figure S5) from prior studies.[37] One can see from Figure 3 that interfacial charge transfer did occur from BP to metals, with 0.23, 0.12, and 0.02 electrons gained per metal atom of Pt, Au, and Ag, respectively. Note that this trend is consistent with the change of metal binding energy in XPS measurements, which is 0.53, 0.21, and 0.15 eV for Pt, Au, and Ag, respectively, as compared to the carbon-supported counterparts (Figure 2).

The electrocatalytic activity of the obtained samples toward ORR was then examined by electrochemical measurements. Figure 4a depicts the rotating ring-disk electrode (RRDE) voltammograms of Pt-TLBP and Pt-CB in an oxygen-saturated 0.1 M KOH. The onset potential (E_{onset}, defined as the electrode potential at the current density j = 0.1 mA/cm^2) of the Pt-TLBP sample was estimated to be +0.970 V vs RHE, about 21 mV more negative than that of Pt-CB (+0.991 V), and the half-wave potential ($E_{1/2}$) of Pt-TLBP was found at +0.747 V, 47 mV more negative than that (+0.794 V) of Pt-CB. The number of electron transfer (n) and hydrogen peroxide yield (H_2O_2%) was then derived from the RRDE profiles (details in the Supporting Information). From Figure 4b, it can be seen that Pt-CB exhibited somewhat higher n values and lower H_2O_2% yield than Pt-TLBP. For instance, the n/H_2O_2% values at +0.7 V were 3.99/0.47% for Pt-CB and

DOI: 10.1021/acsami.9b05471
ACS Appl. Mater. Interfaces 2019, 11, 24707−24714

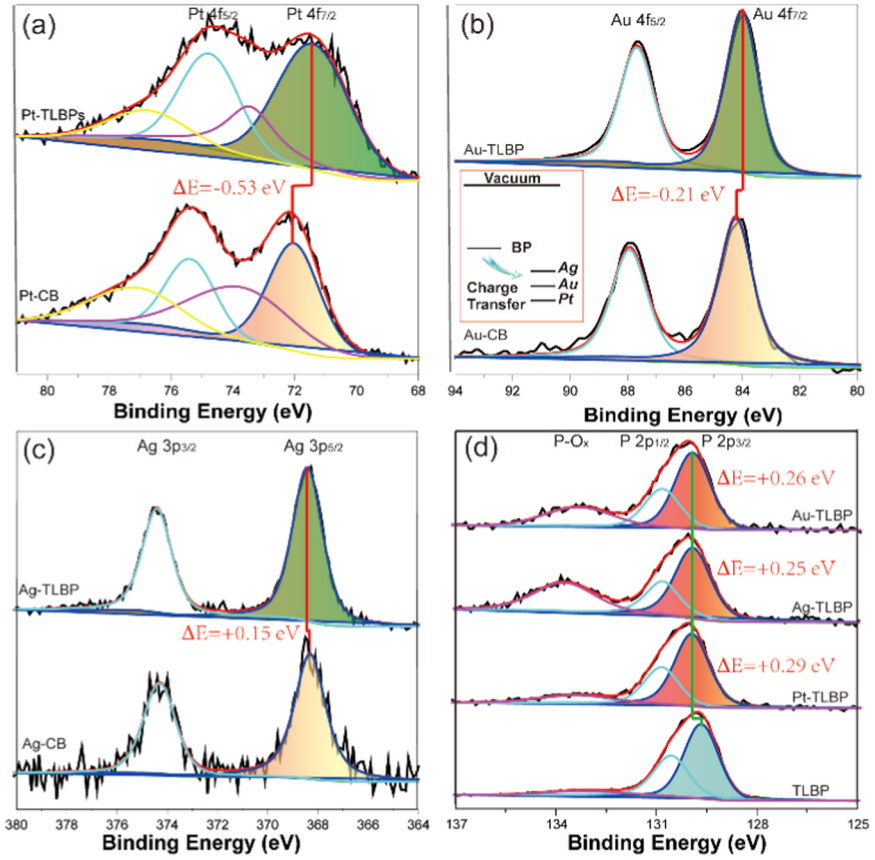

Figure 2. High-resolution XPS profiles of (a) Pt 4f, (b) Au 4f, (c) Ag 3d, and (d) P 2p electrons in M-TLBP and M-CB. Experimental data are shown in the black curves, and deconvolution fits are the colored ones. The shadowed ones are highlighted for comparison. The inset to panel (b) is a schematic diagram showing charge transfer from TLBP to MNPs.

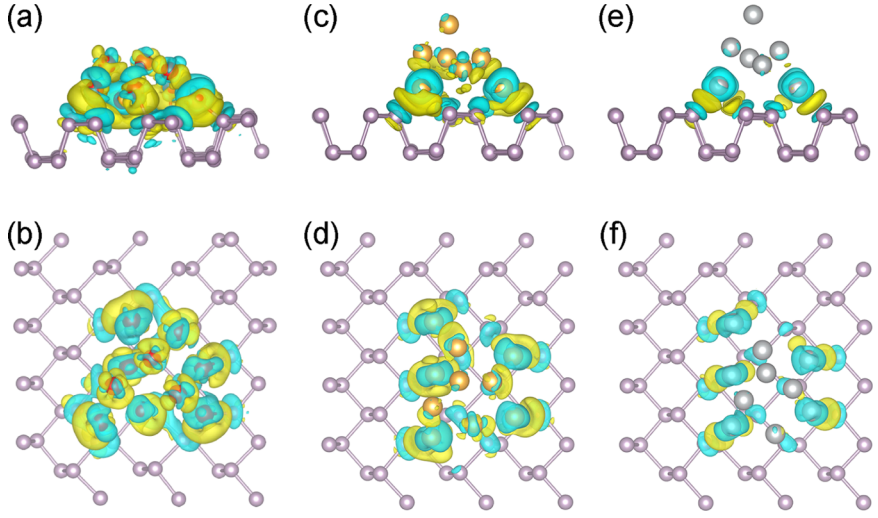

Figure 3. DFT calculations of charge transfer from BP to supported metal nanoparticles: (top) front view and (bottom) top view. (a, b) Pt-BP; (c, d) Au-BP; and (e, f) Ag-BP. The cyan and yellow areas signify electron loss and electron gain, respectively. The isosurface value is set at 0.003 e/au^3.

3.93/3.59% for Pt-TLBP. In addition, the Tafel plots (Figure 4c) showed that the kinetic current density of Pt-CB was markedly higher than that of Pt-TLBP within a rather wide range of electrode potential. These observations suggest that Pt-CB actually outperformed Pt-TLBP toward ORR. This can be accounted for by charge transfer from BP to Pt that strengthened the interaction with oxygen species and hence diminished the ORR activity.

By contrast, markedly enhanced ORR performance was observed with Ag-TLBP and Au-TLBP, as compared to that with Ag-CB and Au-CB. For instance, from Figure 4d, one can see that the E_{onset}'s of Ag-TLBP and Ag-CB were +0.870 and +0.851 V, and $E_{1/2}$'s were +0.694 and +0.648 V, respectively.

DOI: 10.1021/acsami.9b05471
ACS Appl. Mater. Interfaces 2019, 11, 24707−24714

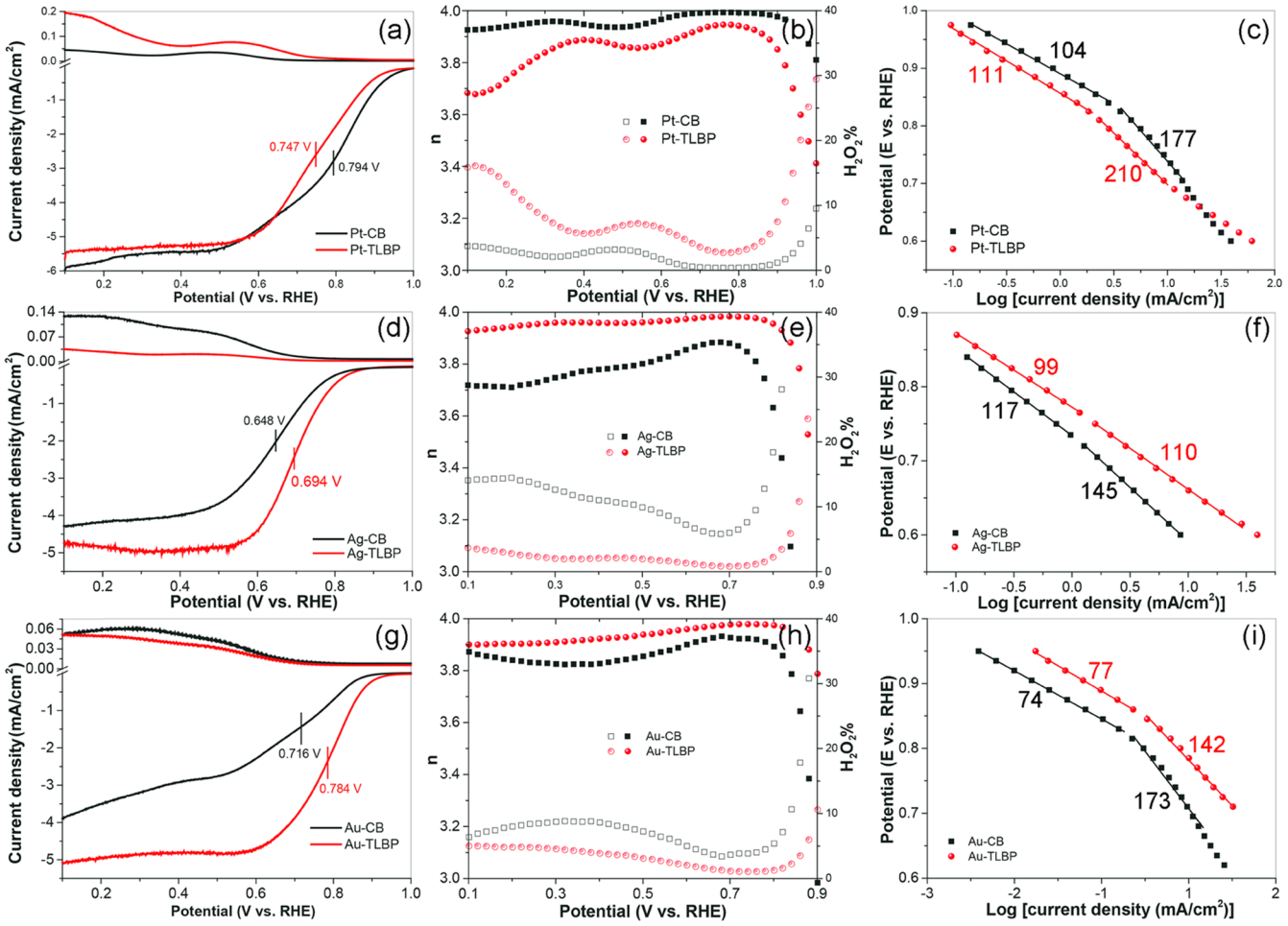

Figure 4. ORR performance of M-TLBP and M-CB in 0.1 M KOH. RRDE voltammograms of (a) Pt-TLBP and Pt-CB, (d) Ag-TLBP and Ag-CB, and (g) Au-TLBP and Au-CB at the rotation rate of 1600 rpm with the ring potential set at +1.5 V vs RHE. (b, e, h) Corresponding electron-transfer number (n, solid) and hydrogen peroxide yield (H_2O_2%, open), and (c, f, i) the Tafel plots with the slopes shown in mV/dec.

For Au-TLBP, the E_{onset} (+0.929 V) was 48 mV higher and $E_{1/2}$ 68 mV higher than those of Au-CB (Figure 4g). In addition, Ag-TLBP (Figure 4e) and Au-TLBP (Figure 4h) also showed higher n and lower H_2O_2% yields than Ag-CB and Au-CB, respectively. Consistent behaviors were observed in the respective Tafel plots (Figure 4f,i), where the kinetic current density of the TLBP-supported samples was markedly higher than those with CB support. These suggest that for Ag and Au, electron transfer from TLBP to the metal nanoparticles actually enhanced the ORR performance, likely due to strengthened binding of oxygen species.

From Figure 5a, one can see that in comparison to M-CB, the mass activity at the potential of +0.80 V increased by 99% for Ag-TLBP and 164% for Au-TLBP but decreased by 50% for Pt-TLBP (the trend was the same for the specific activity, Figure S6). Similarly, the $E_{1/2}$ of Ag-TLBP and Au-TLBP shifted positively by 46 and 90 mV, respectively, while Pt-TLBP shifted negatively by 47 mV, compared to the respective M-CB counterpart (Figure 5b). These can all be ascribed to interfacial charge transfer from TLBP to the supported metal nanoparticles that has been quantified by XPS measurements and DFT calculations (Figure 5c,d). Such a correlation between the ORR performance and electronic property can be understood within the volcano plot framework. As shown in Figure 5e, an increased electron density of Pt pushes the ORR activity further downhill, as the binding to oxygen species became too strong, whereas for Au and Ag, increasing electron density pushes the ORR activity uphill due to enhanced binding to the oxygen intermediates.[57−60]

As mentioned earlier (Figure 1), the metal nanoparticles differed in size between the M-TLBP and M-CB series. Yet, as the sizes are all sufficiently large, the electronic properties of the nanoparticles are anticipated to be similar to those of their respective bulk form.[61−63] Thus, a minimal contribution is anticipated from the disparity of the nanoparticle size to the ORR performance.

CONCLUSIONS

Results from this study show that BP can indeed serve as a unique supporting substrate for metal nanoparticles, where interfacial charge transfer from BP to the supported metals can be exploited as an effective parameter in the manipulation of the electronic interactions with reaction intermediates and hence the electrocatalytic activity toward ORR. Such a behavior is consistent with the volcano plot framework. It is envisaged that the fundamental insights can therefore be extended to the rational design and engineering of metal catalysts for other important reactions in electrochemical energy technologies, and the manipulation will become particularly powerful for atomically dispersed metal catalysts where the metal−substrate interaction is maximized.[64,65]

DOI: 10.1021/acsami.9b05471
ACS Appl. Mater. Interfaces 2019, 11, 24707−24714

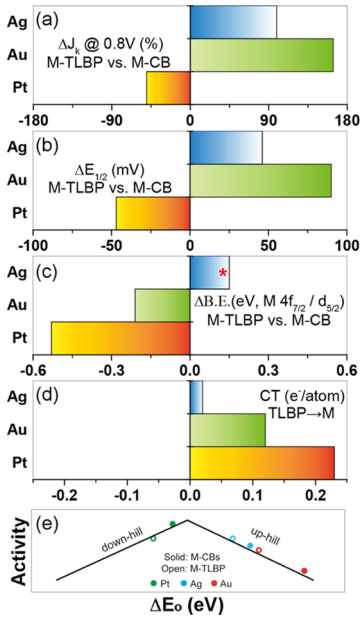

Figure 5. Comparative summary of ORR performance between M-TLBP and M-CB (or TLMP). Changes of (a) kinetic current density (J_k) at +0.8 V, (b) half-wave potential ($E_{1/2}$), (c) binding energy (ΔBE) of the Pt $4f_{7/2}$, Au $4f_{7/2}$, and Ag $3d_{5/2}$ electrons between M-TLBP and M-CB, and P $2p_{3/2}$ electrons between M-TLBP and TLBP, and (d) charge transfer per metal atom from TLBP derived from DFT calculations. (e) Schematic illustration of the effects of BP on the metal ORR performance within the volcano plot framework (note the axes are not in scale).

■ ASSOCIATED CONTENT

Supporting Information

The Supporting Information is available free of charge on the ACS Publications website at DOI: 10.1021/acsami.9b05471.

Representative AFM topograph of a TLBP; TEM micrographs of TLBP; XRD patterns of BP and M-TLBP; CV curves; UV−vis absorption spectra of TLBP and M-TLBP; additional electrochemical data; and structural models of M-BP for DFT calculations (PDF)

■ AUTHOR INFORMATION

Corresponding Authors

*E-mail: chunhongli@iphy.ac.cn (C.L.).
*E-mail: shaowei@ucsc.edu (S.C.).

ORCID

Yi Peng: 0000-0002-5319-1336
Yuan Ping: 0000-0002-0123-3389
Shaowei Chen: 0000-0002-3668-8551

Notes

The authors declare no competing financial interest.

■ ACKNOWLEDGMENTS

This work was supported, in part, by the National Science Foundation (CHE-1710408 and CBET-1848841, S.C.), the National Key R&D Program of China (2017YFA0302903 and 2018YFA0305703, C.L.), and a research fellowship from the China Scholarship Council (C.L.). Y.P. acknowledged the support of a Joseph W. Richards Summer Research Fellowship from the Electrochemical Society and a Chancellor's Dissertation Year Fellowship of the University of California-Santa Cruz. XPS and TEM work at the Molecular Foundry and National Center for Electron Microscopy, Lawrence Berkeley National Laboratory, was supported by the Office of Science, Office of Basic Energy Sciences, of the U.S. Department of Energy under contract No. DE-AC02-05CH11231. XRD data were collected by Jesse Hauser using a Rigaku SmartLab X-ray diffractometer that was purchased with a Major Research Instrument grant (DMR-1126845) from the National Science Foundation.

■ REFERENCES

(1) Cheng, F.; Chen, J. Metal-Air Batteries: from Oxygen Reduction Electrochemistry to Cathode Catalysts. *Chem. Soc. Rev.* **2012**, *41*, 2172−2192.

(2) Debe, M. K. Electrocatalyst Approaches and Challenges for Automotive Fuel Cells. *Nature* **2012**, *486*, 43−51.

(3) Seh, Z. W.; Kibsgaard, J.; Dickens, C. F.; Chorkendorff, I. B.; Norskov, J. K.; Jaramillo, T. F. Combining Theory and Experiment in Electrocatalysis: Insights into Materials Design. *Science* **2017**, *355*, No. eaad4998.

(4) Fan, Z. X.; Zhang, H. Crystal Phase-Controlled Synthesis, Properties and Applications of Noble Metal Nanomaterials. *Chem. Soc. Rev.* **2016**, *45*, 63−82.

(5) Gilroy, K. D.; Ruditskiy, A.; Peng, H. C.; Qin, D.; Xia, Y. N. Bimetallic Nanocrystals: Syntheses, Properties, and Applications. *Chem. Rev.* **2016**, *116*, 10414−10472.

(6) Greeley, J.; Stephens, I. E. L.; Bondarenko, A. S.; Johansson, T. P.; Hansen, H. A.; Jaramillo, T. F.; Rossmeisl, J.; Chorkendorff, I.; Norskov, J. K. Alloys of Platinum and Early Transition Metals as Oxygen Reduction Electrocatalysts. *Nat. Chem.* **2009**, *1*, 552−556.

(7) Nørskov, J. K.; Rossmeisl, J.; Logadottir, A.; Lindqvist, L.; Kitchin, J. R.; Bligaard, T.; Jonsson, H. Origin of the Overpotential for Oxygen Reduction at a Fuel-Cell Cathode. *J. Phys. Chem. B* **2004**, *108*, 17886−17892.

(8) Stamenkovic, V.; Mun, B. S.; Mayrhofer, K. J. J.; Ross, P. N.; Markovic, N. M.; Rossmeisl, J.; Greeley, J.; Norskov, J. K. Changing the Activity of Electrocatalysts for Oxygen Reduction by Tuning the Surface Electronic Structure. *Angew. Chem., Int. Ed.* **2006**, *45*, 2897−2901.

(9) Kulkarni, A.; Siahrostami, S.; Patel, A.; Norskov, J. K. Understanding Catalytic Activity Trends in the Oxygen Reduction Reaction. *Chem. Rev.* **2018**, *118*, 2302−2312.

(10) Peng, Y.; Chen, S. Electrocatalysts Based on Metal@Carbon Core@Shell Nanocomposites: an Overview. *Green Energy Environ.* **2018**, *3*, 335−351.

(11) Deng, J.; Deng, D. H.; Bao, X. H. Robust Catalysis on 2D Materials Encapsulating Metals: Concept, Application, and Perspective. *Adv. Mater.* **2017**, *29*, No. 1606967.

(12) Zhu, Y. P.; Guo, C. X.; Zheng, Y.; Qiao, S. Z. Surface and Interface Engineering of Noble-Metal-Free Electrocatalysts for Efficient Energy Conversion Processes. *Acc. Chem. Res.* **2017**, *50*, 915−923.

(13) Cheng, N. C.; Banis, M. N.; Liu, J.; Riese, A.; Li, X.; Li, R. Y.; Ye, S. Y.; Knights, S.; Sun, X. L. Extremely Stable Platinum Nanoparticles Encapsulated in a Zirconia Nanocage by Area-Selective Atomic Layer Deposition for the Oxygen Reduction Reaction. *Adv. Mater.* **2015**, *27*, 277−281.

(14) Gunji, T.; Saravanan, G.; Tanabe, T.; Tsuda, T.; Miyauchi, M.; Kobayashi, G.; Abe, H.; Matsumoto, F. Long-Term, Stable, and Improved Oxygen-Reduction Performance of Titania-supported PtPb Nanoparticles. *Catal. Sci. Technol.* **2014**, *4*, 1436−1445.

(15) Tian, X. L.; Luo, J. M.; Nan, H. X.; Zou, H. B.; Chen, R.; Shu, T.; Li, X. H.; Li, Y. W.; Song, H. Y.; Liao, S. J.; Adzic, R. R. Transition Metal Nitride Coated with Atomic Layers of Pt as a Low-Cost, Highly Stable Electrocatalyst for the Oxygen Reduction Reaction. *J. Am. Chem. Soc.* **2016**, *138*, 1575−1583.

DOI: 10.1021/acsami.9b05471
ACS Appl. Mater. Interfaces 2019, 11, 24707−24714

(16) Du, L.; Shao, Y. Y.; Sun, J. M.; Yin, G. P.; Liu, J.; Wang, Y. Advanced Catalyst Supports for PEM Fuel Cell Cathodes. *Nano Energy* **2016**, *29*, 314−322.
(17) Song, Y.; Chen, S. W. Graphene Quantum-Dot-Supported Platinum Nanoparticles: Defect-Mediated Electrocatalytic Activity in Oxygen Reduction. *ACS Appl. Mater. Interfaces* **2014**, *6*, 14050−14060.
(18) He, G. Q.; Song, Y.; Liu, K.; Walter, A.; Chen, S.; Chen, S. W. Oxygen Reduction Catalyzed by Platinum Nanoparticles Supported on Graphene Quantum Dots. *ACS Catal.* **2013**, *3*, 831−838.
(19) Deming, C. P.; Mercado, R.; Gadiraju, V.; Sweeney, S. W.; Khan, M.; Chen, S. W. Graphene Quantum Dots-Supported Palladium Nanoparticles for Efficient Electrocatalytic Reduction of Oxygen in Alkaline Media. *ACS Sustainable Chem. Eng.* **2015**, *3*, 3315−3323.
(20) Chen, L. M.; Peng, Y.; Lu, J. E.; Wang, N.; Hu, P. G.; Lu, B. Z.; Chen, S. W. Platinum Nanoparticles Encapsulated in Nitrogen-Doped Graphene Quantum Dots: Enhanced Electrocatalytic Reduction of Oxygen by Nitrogen Dopants. *Int. J. Hydrogen Energy* **2017**, *42*, 29192−29200.
(21) Sofer, Z.; Sedmidubsky, D.; Huber, S.; Luxa, J.; Bousa, D.; Boothroyd, C.; Pumera, M. Layered Black Phosphorus: Strongly Anisotropic Magnetic, Electronic, and Electron-Transfer Properties. *Angew. Chem., Int. Ed.* **2016**, *55*, 3382−3386.
(22) Batmunkh, M.; Bat-Erdene, M.; Shapter, J. G. Phosphorene and Phosphorene-Based Materials - Prospects for Future Applications. *Adv. Mater.* **2016**, *28*, 8586−8617.
(23) He, R.; Hua, J.; Zhang, A. Q.; Wang, C. H.; Peng, J. Y.; Chen, W. J.; Zeng, J. Molybdenum Disulfide-Black Phosphorus Hybrid Nanosheets as a Superior Catalyst for Electrochemical Hydrogen Evolution. *Nano Lett.* **2017**, *17*, 4311−4316.
(24) Luo, Z. Z.; Zhang, Y.; Zhang, C. H.; Tan, H. T.; Li, Z.; Abutaha, A.; Wu, X. L.; Xiong, Q. H.; Khor, K. A.; Hippalgaonkar, K.; Xu, J. W.; Hng, H. H.; Yan, Q. Y. Multifunctional 0D-2D Ni2P Nanocrystals-Black Phosphorus Heterostructure. *Adv. Energy Mater.* **2017**, *7*, No. 1601285.
(25) Pang, J. B.; Bachmatiuk, A.; Yin, Y.; Trzebicka, B.; Zhao, L.; Fu, L.; Mendes, R. G.; Gemming, T.; Liu, Z. F.; Rummeli, M. H. Applications of Phosphorene and Black Phosphorus in Energy Conversion and Storage Devices. *Adv. Energy Mater.* **2018**, *8*, No. 1702093.
(26) Xue, Y. H.; Zhang, Q.; Zhang, T.; Fu, L. Black Phosphorus: Properties, Synthesis, and Applications in Energy Conversion and Storage. *ChemNanoMat* **2017**, *3*, 352−361.
(27) Ren, X. L.; Lian, P. C.; Xie, D. L.; Yang, Y.; Mei, Y.; Huang, X. R.; Wang, Z. R.; Yin, X. T. Properties, Preparation and Application of Black Phosphorus/Phosphorene for Energy Storage: a Review. *J. Mater. Sci.* **2017**, *52*, 10364−10386.
(28) Ran, J. R.; Zhu, B. C.; Qiao, S. Z. Phosphorene Co-catalyst Advancing Highly Efficient Visible-Light Photocatalytic Hydrogen Production. *Angew. Chem., Int. Ed.* **2017**, *56*, 10373−10377.
(29) Wu, T.; Fan, J. C.; Li, Q. X.; Shi, P. H.; Xu, Q. J.; Min, Y. L. Palladium Nanoparticles Anchored on Anatase Titanium Dioxide-Black Phosphorus Hybrids with Heterointerfaces: Highly Electroactive and Durable Catalysts for Ethanol Electrooxidation. *Adv. Energy Mater.* **2018**, *8*, No. 1701799.
(30) Li, C. H.; Long, Y. J.; Zhao, L. X.; Shan, L.; Ren, Z. A.; Zhao, J. Z.; Weng, H. M.; Dai, X.; Fang, Z.; Ren, C.; Chen, G. F. Pressure-Induced Topological Phase Transitions and Strongly Anisotropic Magnetoresistance in Bulk Black Phosphorus. *Phys. Rev. B* **2017**, *95*, No. 125417.
(31) Nilges, T.; Kersting, M.; Pfeifer, T. A Fast Low-Pressure Transport Route to Large Black Phosphorus Single Crystals. *J. Solid State Chem.* **2008**, *181*, 1707−1711.
(32) Giannozzi, P.; Baroni, S.; Bonini, N.; Calandra, M.; Car, R.; Cavazzoni, C.; Ceresoli, D.; Chiarotti, G. L.; Cococcioni, M.; Dabo, I.; Dal Corso, A.; de Gironcoli, S.; Fabris, S.; Fratesi, G.; Gebauer, R.; Gerstmann, U.; Gougoussis, C.; Kokalj, A.; Lazzeri, M.; Martin-Samos, L.; Marzari, N.; Mauri, F.; Mazzarello, R.; Paolini, S.; Pasquarello, A.; Paulatto, L.; Sbraccia, C.; Scandolo, S.; Sclauzero, G.; Seitsonen, A. P.; Smogunov, A.; Umari, P.; Wentzcovitch, R. M. QUANTUM ESPRESSO: a Modular and Open-Source Software Project for Quantum Simulations of Materials. *J. Phys.: Condens. Matter* **2009**, *21*, No. 395502.
(33) Garrity, K. F.; Bennett, J. W.; Rabe, K. M.; Vanderbilt, D. Pseudopotentials for high-throughput DFT calculations. *Comput. Mater. Sci.* **2014**, *81*, 446−452.
(34) Marzari, N.; Vanderbilt, D.; De Vita, A.; Payne, M. C. Thermal Contraction and Disordering of the Al(110) Surface. *Phys. Rev. Lett.* **1999**, *82*, 3296−3299.
(35) Grimme, S. Semiempirical GGA-Type Density Functional Constructed with a Long-Range Dispersion Correction. *J. Comput. Chem.* **2006**, *27*, 1787−1799.
(36) Barone, V.; Casarin, M.; Forrer, D.; Pavone, M.; Sambi, M.; Vittadini, A. Role and Effective Treatment of Dispersive Forces in Materials: Polyethylene and Graphite Crystals as Test Cases. *J. Comput. Chem.* **2009**, *30*, 934−939.
(37) Bai, L.; Wang, X.; Tang, S.; Kang, Y.; Wang, J.; Yu, Y.; Zhou, Z. K.; Ma, C.; Zhang, X.; Jiang, J.; Chu, P. K.; Yu, X. F. Black Phosphorus/Platinum Heterostructure: A Highly Efficient Photocatalyst for Solar-Driven Chemical Reactions. *Adv. Mater.* **2018**, No. e1803641.
(38) Zhang, X.; Xie, H. M.; Liu, Z. D.; Tan, C. L.; Luo, Z. M.; Li, H.; Lin, J. D.; Sun, L. Q.; Chen, W.; Xu, Z. C.; Xie, L. H.; Huang, W.; Zhang, H. Black Phosphorus Quantum Dots. *Angew. Chem., Int. Ed.* **2015**, *54*, 3653−3657.
(39) Sun, Z. B.; Xie, H. H.; Tang, S. Y.; Yu, X. F.; Guo, Z. N.; Shao, J. D.; Zhang, H.; Huang, H.; Wang, H. Y.; Chu, P. K. Ultrasmall Black Phosphorus Quantum Dots: Synthesis and Use as Photothermal Agents. *Angew. Chem., Int. Ed.* **2015**, *54*, 11526−11530.
(40) Lee, K. S.; El-Sayed, M. A. Gold and silver nanoparticles in sensing and imaging: Sensitivity of plasmon response to size, shape, and metal composition. *J. Phys. Chem. B* **2006**, *110*, 19220−19225.
(41) Hutter, E.; Fendler, J. H.; Roy, D. Surface Plasmon Resonance Studies of Gold and Silver Nanoparticles Linked to Gold and Silver Substrates by 2-Aminoethanethiol and 1,6-Hexanedithiol. *J. Phys. Chem. B* **2001**, *105*, 11159−11168.
(42) Choi, S.; Lee, H. J.; Oh, M. Facile Synthesis of Au or Ag Nanoparticles-Embedded Hollow Carbon Microspheres from Metal-Organic Framework Hybrids and Their Efficient Catalytic Activities. *Small* **2016**, *12*, 2425−2431.
(43) Farrag, M. Monodisperse and Polydisperse Platinum Nanoclusters Supported over TiO2 Anatase as Catalysts for Catalytic Oxdation of Styrene. *J. Mol. Catal. A: Chem.* **2016**, *413*, 67−76.
(44) Dukovic, G.; Merkle, M. G.; Nelson, J. H.; Hughes, S. M.; Alivisatos, A. P. Photodeposition of Pt on Colloidal CdS and CdSe/CdS Semiconductor Nanostructures. *Adv. Mater.* **2008**, *20*, 4306−4311.
(45) Zheng, Z. K.; Huang, B. B.; Qin, X. Y.; Zhang, X. Y.; Dai, Y.; Whangbo, M. H. Facile in situ Synthesis of Visible-Light Plasmonic Photocatalysts M@TiO2 (M = Au, Pt, Ag) and Evaluation of Their Photocatalytic Oxidation of Benzene to Phenol. *J. Mater. Chem.* **2011**, *21*, 9079−9087.
(46) Murdoch, M.; Waterhouse, G. I. N.; Nadeem, M. A.; Metson, J. B.; Keane, M. A.; Howe, R. F.; Llorca, J.; Idriss, H. The Effect of Gold Loading and Particle Size on Photocatalytic Hydrogen Production from Ethanol over Au/TiO2 Nanoparticles. *Nat. Chem.* **2011**, *3*, 489−492.
(47) Gui, R.; Jin, H.; Wang, Z. H.; Li, J. H. Black Phosphorus Quantum Dots: Synthesis, Properties, Functionalized Modification and Applications. *Chem. Soc. Rev.* **2018**, *47*, 6795−6823.
(48) Zhu, M. S.; Kim, S.; Mao, L.; Fujitsuka, M.; Zhang, J. Y.; Wang, X. C.; Majima, T. Metal-Free Photocatalyst for H-2 Evolution in Visible to Near-Infrared Region: Black Phosphorus/Graphitic Carbon Nitride. *J. Am. Chem. Soc.* **2017**, *139*, 13234−13242.
(49) Fantauzzi, D.; Calderon, S. K.; Mueller, J. E.; Grabau, M.; Papp, C.; Steinruck, H. P.; Senftle, T. P.; van Duin, A. C. T.; Jacob, T.

DOI: 10.1021/acsami.9b05471
ACS Appl. Mater. Interfaces 2019, 11, 24707−24714

Growth of Stable Surface Oxides on Pt(111) at Near-Ambient Pressures. *Angew. Chem., Int. Ed.* **2017**, *56*, 2594−2598.
(50) Tang, H. L.; Su, Y.; Zhang, B. S.; Lee, A. F.; Isaacs, M. A.; Wilson, K.; Li, L.; Ren, Y. G.; Huang, J. H.; Haruta, M.; Qiao, B. T.; Liu, X.; Jin, C. Z.; Su, D. S.; Wang, J. H.; Zhang, T. Classical Strong Metal-Support Interactions between Gold Nanoparticles and Titanium Dioxide. *Sci. Adv.* **2017**, *3*, No. e1700231.
(51) Chen, L. M.; Deming, C. P.; Peng, Y.; Hu, P. G.; Stofan, J.; Chen, S. W. Gold Core@Silver Semishell Janus Nanoparticles Prepared by Interfacial Etching. *Nanoscale* **2016**, *8*, 14565−14572.
(52) Song, Y.; Liu, K.; Chen, S. W. AgAu Bimetallic Janus Nanoparticles and Their Electrocatalytic Activity for Oxygen Reduction in Alkaline Media. *Langmuir* **2012**, *28*, 17143−17152.
(53) Zhu, X. J.; Zhang, T. M.; Sun, Z. J.; Chen, H. L.; Guan, J.; Chen, X.; Ji, H. X.; Du, P. W.; Yang, S. F. Black Phosphorus Revisited: A Missing Metal-Free Elemental Photocatalyst for Visible Light Hydrogen Evolution. *Adv. Mater.* **2017**, *29*, No. 1605776.
(54) Ryder, C. R.; Wood, J. D.; Wells, S. A.; Yang, Y.; Jariwala, D.; Marks, T. J.; Schatz, G. C.; Hersam, M. C. Covalent Functionalization and Passivation of Exfoliated Black Phosphorus via Aryl Diazonium Chemistry. *Nat. Chem.* **2016**, *8*, 597−602.
(55) Liu, Y. Y.; Stradins, P.; Wei, S. H. Van der Waals Metal-Semiconductor Junction: Weak Fermi Level Pinning Enables Effective Tuning of Schottky Barrier. *Sci. Adv.* **2016**, *2*, No. e1600069.
(56) Cai, Y. Q.; Zhang, G.; Zhang, Y. W. Layer-dependent Band Alignment and Work Function of Few-Layer Phosphorene. *Sci. Rep.* **2014**, *4*, No. 6677.
(57) Wang, L. K.; Tang, Z. H.; Yan, W.; Yang, H. Y.; Wang, Q. N.; Chen, S. W. Porous Carbon-Supported Gold Nanoparticles for Oxygen Reduction Reaction: Effects of Nanoparticle Size. *ACS Appl. Mater. Interfaces* **2016**, *8*, 20635−20641.
(58) Stamenkovic, V. R.; Fowler, B.; Mun, B. S.; Wang, G. F.; Ross, P. N.; Lucas, C. A.; Markovic, N. M. Improved Oxygen Reduction Activity on Pt3Ni(111) via Increased Surface Site Availability. *Science* **2007**, *315*, 493−497.
(59) Chang, J. F.; Feng, L. G.; Liu, C. P.; Xing, W.; Hu, X. L. Ni2P Enhances the Activity and Durability of the Pt Anode Catalyst in Direct Methanol Fuel Cells. *Energy Environ. Sci.* **2014**, *7*, 1628−1632.
(60) Xu, B.; Zhou, G.; Wang, X. Rational Synthesis and the Structure-Property Relationships of Nanoheterostructures: a Combinative Study of Experiments and Theory. *NPG Asia Mater.* **2015**, *7*, No. e164.
(61) Shao, M. H.; Peles, A.; Shoemaker, K. Electrocatalysis on Platinum Nanoparticles: Particle Size Effect on Oxygen Reduction Reaction Activity. *Nano Lett.* **2011**, *11*, 3714−3719.
(62) Lu, Y. Z.; Chen, W. Size Effect of Silver Nanoclusters on Their Catalytic Activity for Oxygen Electro-Reduction. *J. Power Sources* **2012**, *197*, 107−110.
(63) Chen, W.; Chen, S. W. Oxygen Electroreduction Catalyzed by Gold Nanoclusters: Strong Core Size Effects. *Angew. Chem., Int. Ed.* **2009**, *48*, 4386−4389.
(64) Zhang, G. X.; Jia, Y.; Zhang, C.; Xiong, X. Y.; Sun, K.; Chen, R. D.; Chen, W. X.; Kuang, Y.; Zheng, L. R.; Tang, H. L.; Liu, W.; Liu, J. F.; Sun, X. M.; Lin, W. F.; Dai, H. J. A General Route via Formamide Condensation to Prepare Atomically Dispersed Metal-Nitrogen-Carbon Electrocatalysts for Energy Technologies. *Energy Environ. Sci.* **2019**, *12*, 1317−1325.
(65) Peng, Y.; Lu, B. Z.; Chen, S. W. Carbon-Supported Single Atom Catalysts for Electrochemical Energy Conversion and Storage. *Adv. Mater.* **2018**, *30*, No. 1801995.

DOI: 10.1021/acsami.9b05471
ACS Appl. Mater. Interfaces 2019, 11, 24707−24714